3D analysis of ceramic powder sintering by synchrotron X-ray nano-tomography

Aatreya Manjulagiri Venkatesh, Didier Bouvard, Pierre Lhuissier, Julie Villanova

3D Analysis of Ceramic Powder Sintering by Synchrotron X-ray Nano-tomography

Aatreya Manjulagiri Venkatesh [a], Didier Bouvard [b], Pierre Lhuissier [c], Julie Villanova [d]

[a] Univ. Grenoble Alpes, CNRS, Grenoble INP, SIMAP, 38000 Grenoble, France, mvaatreya@gmail.com

[b] Univ. Grenoble Alpes, CNRS, Grenoble INP, SIMAP, 38000 Grenoble, France, didier.bouvard@grenoble-inp.fr

[c] Univ. Grenoble Alpes, CNRS, Grenoble INP, SIMAP, 38000 Grenoble, France, pierre.lhuissier@simap.grenoble-inp.fr

[d] ESRF - The European Synchrotron, 71 Avenue des Martyrs, 38000 Grenoble, France, julie.villanova@esrf.fr

Abstract

In-depth investigation of the sintering phenomena in ceramic powders remains challenging, with the typical size of the individual particles being around 1 μm or less, i.e., at the resolution limit of X-ray micro-tomography (μCT). This has been dealt with, thanks to the state-of-the-art hard X-ray nano-analysis beamline at the upgraded European Synchrotron Radiation Facility (ESRF). Complete 3D images were obtained for representative ceramic powder systems with a voxel size as low as 25 nm, so as to depict particles and pores with adequate details and follow the entire sintering process. Subsequent quantitative image analyses were used to explore microstructural changes, including the evolution of relevant sintering parameters with respect to the grains and the pores. Notably, a study adopted in this research on the advancement of pore curvatures can be linked to tracking the stages of sintering.

Keywords

Sintering; Ceramic powders; Synchrotron X-ray nano-tomography; Quantitative image analysis; Grain growth; Pore size distribution; Pore curvature.

1. Introduction

Sintering is undoubtedly the most prominent step in powder processing of ceramics [1], involving the transformation of a powder or a powder compact into a bulk material of controlled density under thermal energy. The complete process is classically divided into three sequential and overlapping stages, characterized by the formation of so-called necks in between the individual

particles in the initial stage, considerable densification resulting from the shrinkage of the interconnected pore channels in the intermediate stage, and eventually the creation of isolated closed pores in the final stage, with concomitant grain growth [2] [3].

The experimental studies in the context of powder sintering and the subsequent characterization for a quantitative investigation were largely carried out by classical observation techniques such as optical or scanning electron microscopy (SEM). The micrographs of the traditional SEMs were vital in illustrating various sintering related phenomena, but, from a two-dimensional (2D) perspective with relatively small fields of view. This restricted the assessments of complex sintering parameters, which require rather a three-dimensional (3D) outlook [4]. For instance, 2D images provide insufficient understanding of the complex network of pore morphologies in a microstructure. The 3D interconnected pore channels could appear isolated in 2D sections, giving insufficient or wrong impression on the connectivity and the closure of the pores [5] [6]. This highlights the significance of 3D imaging offered by non-conventional characterization techniques, like X-ray tomography.

In fact, 3D imaging has been proven to be of great value in improving the understanding and modeling of sintering of metallic and glass powders. Various notable works of Lame *et al.* [7], Nöthe *et al.* [8], Olmos *et al.* [9], and Kieback *et al.* [10] have employed X-ray micro-tomography (μCT) apparatus to compute and follow-up relevant sintering parameters. These works, for instance, have employed a resolution of around 1.5 μm pixel size to detect critical sintering related features in the metallic particles of approximately 50 μm in size. This ratio of the order of 1/20 to 1/40 between the resolution and particle size has been found to be a good trade-off amongst the high resolution required to precisely quantify necks and curvatures and the low resolution required to capture particle agglomeration and rearrangement. The insights offered by the characterization of various such tomography outcomes were also found to better validate the sintering theories, as the ones proposed by Delannay *et al.* [11].

For ceramic powders, the same results cannot be realized as a considerably higher resolution is required to enable particle scale imaging. Indeed, as a result of their small size (around or below 1 μm) and complex architecture, ceramic particles most often form agglomerates. Consequently, prominent X-ray μCT studies over the last two decades on ceramic samples by Bernard *et al.* [12], Lu *et al.* [13], Xu *et al.* [14] etc. to visualize and quantify microstructural evolutions during

sintering have been restricted to the agglomerate level. However, more recently, with the advancement in the X-ray nano-tomography (nano-CT) domain at the synchrotron facilities, microstructural evolutions during sintering at the nano-scale are being investigated, as in Okuma *et al.* [15], paving the way for comprehensive ceramic studies. Particularly remarkable has been the observation of sintering phenomena of glass beads at a sintering temperature of 670°C [16]. Nevertheless, it is worth noting that the analyses of commonly used ceramic powders are more delicate because of the higher temperatures required (around or more than 1500°C). To the best of our knowledge, none of the various types of tomography, be it post-mortem, ex-situ or in-situ – choosing the terminology proposed by Salvo *et al.* [17] – has been attempted at a resolution good enough for particle length-scale observation of ceramic powder sintering at higher temperatures so far.

In this work, we explore the nano-tomography technique presented by the ID16B nano-analysis beamline at the European synchrotron (ESRF). The beamline offers a phase-contrast based holotomography set-up [18], which allows 3D imaging at the nano-scale (~25 nm voxel size), with fast scan times and with fields of view that are large enough to constitute representative volume elements [19]. With this high resolution, we were able to investigate two sets of pre-sintered micron-sized alumina powders in a post-mortem context. 3D images obtained at this resolution were used to investigate densified versions of the alumina powder compacts as well, thus allowing the analysis of intermediate and final stages of sintering. The subsequent quantitative evaluations were utilized to follow the evolution of the morphologies of the grains and the pores and a few associated parameters at different sintering time intervals. The information obtained was further scrutinized by comparing them with classical analytical sintering theories. Furthermore, given that the curvature changes are the foremost phenomena in the sintering process, high resolution 3D renderings were used to plot and analyze curvature maps from a porosity reference framework. These maps are shown to serve as an indicator to track the evolution of sintering stages.

2. Materials and Methods

2.1 Powder and sample preparation

Two sets of alumina powders, AA-07 and AA-1.3, procured from Sumitomo Chemical Co., Ltd. with mean particle sizes of around 0.7 μm and 1.3 μm, respectively, were chosen. These sizes fit the investigation criteria of the synchrotron experiments in terms of the expected resolution (~25

nm). Preliminary SEM evaluations show that these so-called advanced alumina powders, produced by an aluminium alkoxide hydrolysis process [20] [21], have an almost isotropic, polyhedral shape and are fairly non-agglomerated (Figure 1).

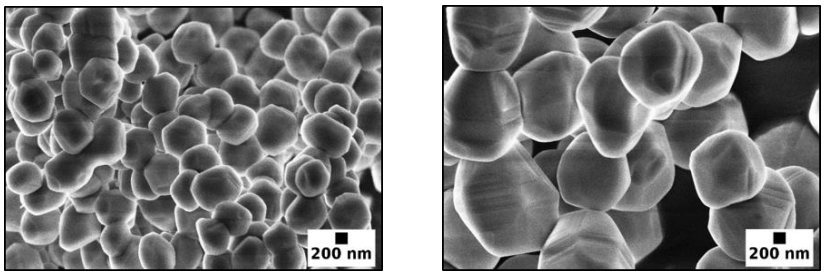

(a) **(b)**

Figure 1. SEM observation of alumina powders with particle sizes of around (a) 0.7 µm and (b) 1.3 µm respectively.

To assess the sintering advancement of the chosen powders, cylindrical compacts (~8 mm in diameter) obtained by uniaxial pressing of the powders in a die with a stress of ~200MPa, were subjected to sintering experiments in a dilatometry set-up in air. Small quantities of polyvinyl alcohol were used as a binder for better compaction. Thermal cycles were imposed on to the powder compacts at a rate of 5°C/min with a sintering plateau at 1500°C. A 1-hour isothermal hold at 500°C was carried out to remove the binder prior to sintering. The powder compacts were then sintered individually for different time periods up to 120 hours at 1500°C, and the shrinkage and densification attained were recorded. Bulk densities of the sintered compacts and therewith their relative densities were determined using the conventional 'Archimedes' principle, with ethanol as the weighting medium. The compacts were further broken into tiny fragments (about 100 µm in diameter and 1-2 mm in height) for a subsequent investigation using the nano-CT.

2.2 Phase-contrast X-ray nano-holotomography

In order to visualize the sintered alumina fragments at the particle scale, X-ray nano-CT experiments were carried out at the ID16B nano-analysis beamline of the ESRF. The beamline is equipped with a set of Kirkpatrick-Baez (KB) mirror systems. These mirrors focus the incoming parallel X-ray beam onto a small beam size of 50*50 nm^2, which acts as a secondary source [19]. The subsequent conic beam advancement results in a geometrical magnification. An energy of 29.2 KeV was used for the experimentations.

With the holotomography system, propagation based phase-contrast imaging was performed by placing and moving the sample (at distance D1) in the conic beam space at 4 different distances relative to the focal plane. For each of the 4 sample-to-focus distances, 3203 projections were recorded over a 360° rotation using a scintillator screen (LSO 17m) and a cMOS detector system (pco.edge 5.5) at a fixed distance D1 + D2 from the focal spot (Figure 2 (a)) [18] [22] [23].

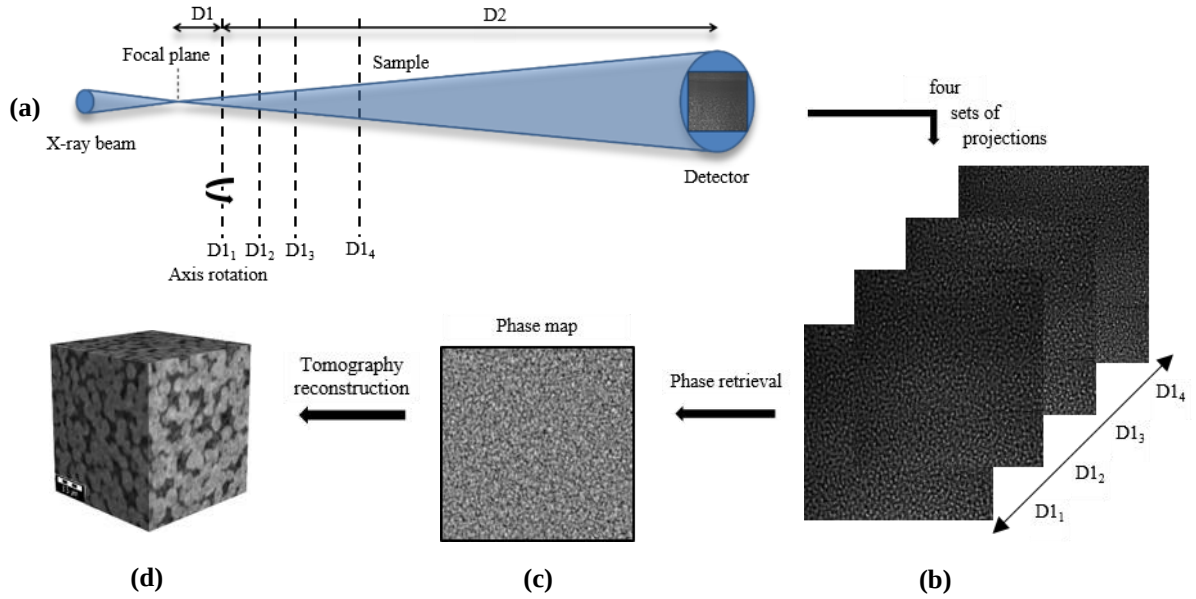

Figure 2. Principle of nano-CT at ID16B beamline of ESRF: (a) sketch of the experimental set-up, (b) radiographs recorded from the 4-distance image set and (c) phase map obtained by phase retrieval, which are then used in (d) a tomographic reconstruction.

The recorded images at $D1_1$ = 29 mm, $D1_2$ = 30 mm, $D1_3$ = 34 mm and $D1_4$ = 44 mm were aligned and magnified according to the first distance image (Figure 2 (b)), resulting in a pixel size of 25 nm and a field of view of 64*64*54 μm^3. The exposure time for each projection was optimized to 50 ms, leading to an acquisition time of ~4 min for 1-distance imaging. The phase shifts undergone by the sample were captured from this 4-distance image set by means of iterative phase retrieval algorithms to obtain the so-called phase maps (Figure 2 (c)). The filtered 2D phase maps were then fed into the in-house built ESRF PyHST2 software package [24] to reconstruct and render the 3D distribution of the sample (Figure 2 (d)).

2.3 Image treatment and analyses

Regions of interest (ROIs) of 1000*1000*1000 voxels were extracted from the reconstructed 3D image stacks. Ring artefacts present were removed with a MATLAB algorithm based on image

filtering [25]. A trial-and-error approach was used to find the appropriate parameters. The ROIs were then pre-processed with filters such as fast Fourier transform filter (cut-off frequency of 5%) to remove high-frequency noise, non-local means filter (strength of 0.5) to reduce left-over noise while keeping the edges sharp etc., in image processing software ImageJ and GeoDict [26] [27]. This was followed by the application of automatic thresholding methodologies (OTSU's method) in order to further integrate the segmented 3D renderings in a quantitative analysis set-up. However, segmentation of individual features, say, the separation of individual sintered grains, was challenging, especially for image stacks above 75-80% density. Parameters requiring only effective pre-processing and global thresholding operations for their evaluation were hence chosen.

Grain volume fraction measurement

Volume fractions of the grains were first determined from the ROIs with the ImageJ software [26], to compare with the relative density estimation from the Archimedes approach.

Grain size and pore size estimation

Next, granulometric analysis in the Geodict image processing platform was employed to estimate the size of the evolving grains [27]. The algorithm in the GrainFind module of GeoDict first converts the thresholded 3D image stacks into distance maps by Euclidean distance transform (EDT) and then evaluates the diameter of the grains by fitting pre-defined spheres into the grain space. A detailed description of the algorithm and its implementation can be found in [28]. Similarly, pore size distributions of the 3D image stacks were carried out by granulometric characterization in the pore space using the PoroDict module of GeoDict [27] [29].

Pore connectivity and pore throat characterization

In order to assess the connectivity in the pore network and their transition into closed porosity, parameters such as pore volume, percentages of open porosity, and percentages of closed porosity were measured using the Analysis_3D plugin in ImageJ [26] [30]. Furthermore, a porosimetric investigation was carried out in the PoroDict module of GeoDict [27] [29]. In contrast to granulometry, here, pre-defined spheres that are fitted into the pore structure are made to pass through from the side of the intrusion to the other side such that it encompasses the entire pore

channel. With this, the size of the small pore channels or throats connecting the large pore channels are determined, while needless to say, closed pores do not contribute to the pore throat analyses.

Interface curvature analysis

To track the evolution of pore-solid interface curvature, simplified henceforth as pore curvature, the tools, 'Shape index' and 'Curvedness' proposed by Koenderink *et al.* [31] for graphical representation of 3D shapes were adopted. In contrast to the classical curvature measures like the Gaussian and the mean curvatures, these shape indicators capture the nuances in the variations of local shapes [32]. The significance of these parameters has been emphasized notably by Shahani *et al.* [33]. They are independent of each other, with the shape index estimating the local shape profile and the curvedness measuring the amount of curvature of the shape. The significance of these indicators will be further explained in section 3.3. With k_1 and k_2 as the principal curvatures, the shape index S and curvedness C are defined as follows:

$$\boldsymbol{S = \frac{2}{\pi}\arctan\left(\frac{k_1 + k_2}{k_1 - k_2}\right)} \quad \textbf{1}$$

$$\boldsymbol{C = \sqrt{\frac{{k_1}^2 + {k_2}^2}{2}}} \quad \textbf{2}$$

The shape index in Equation 1 can have values in the range from -1 to +1, differentiating convexities from concavities. The curvedness instead, in Equation 2, is a positive value, with 0 indicating a planar surface, quantifying the amount of deviation from a flat plane. Taking these indicators into consideration, pore surfaces of the 3D image stacks were first generated in Avizo software package [34]. Principal curvature values were then computed from the generated surfaces. Using these values, the shape indicators were subsequently calculated in a Python environment, to be further applied to plot curvature maps, i.e., 2D density histogram plots in the (S,C) plane.

3. Results

3.1 Global assessment

Detailed microstructural changes undergone by the sintered materials were revealed, thanks to the high resolution and the large field of view resulting from the multiple distance phase retrieval.

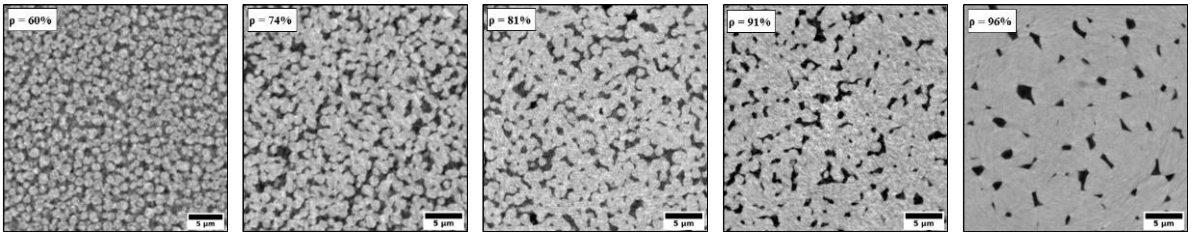

(a) (b) (c) (d) (e)

Figure 3. One of the cross-section slices of the 3D reconstructed alumina samples of 1.3 µm (a), sintered at 1500°C and observed post-mortem after (b) 1 hour, (c) 10 hours, (d) 30 hours and (e) 120 hours respectively. The relative density values 'ρ' are mentioned on top-left. Scale bar is 5 µm. Alumina grains are in gray, while the black phase is porosity.

At a global level, many sintering phenomena such as inter-particle neck growth, densification, grain growth, pore rounding, etc. that are stated in the traditional sintering theories at different stages of sintering [1] [2] [35] are clearly observed in the two alumina samples. Figure 3 (a) shows one of the cross-section slices taken from the middle of the image stack (1000*1000*1000 voxels) of the 3D reconstructed alumina of 1.3 µm average particle size (henceforth referred to as 'Al 1.3µm'), sintered at 1500°C with an original relative density of around 60%. Over time (Figure 3 (b) (c) (d)), we see developments in this original 'green' sample, such as the growth of inter-particle necks, particle center-to-center shrinkage and a considerable densification, with the Archimedes relative density 'ρ' reaching 74%, 81%, 91% and 96% after 1 hour, 10 hours, 30 hours and 120 hours respectively. The sintered samples thus appear to span the intermediate (~70 to ~90% of density) and the final stage of sintering (above ~90% density).

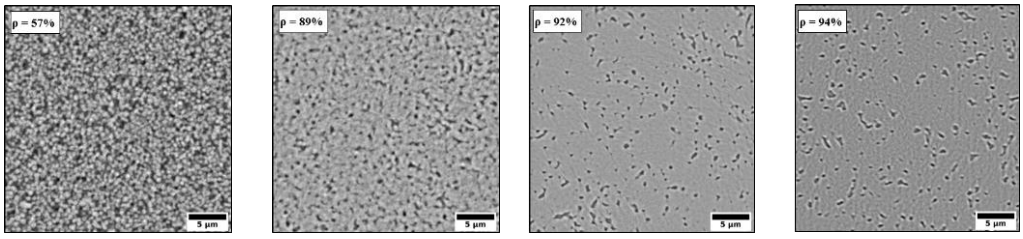

(a) (b) (c) (d)

Figure 4. One of the cross-section slices of the 3D reconstructed alumina samples of 0.7 µm (a), sintered at 1500°C and observed post-mortem after (b) 30 min, (c) 1 hour and (d) 10 hours respectively. The relative density values 'ρ' are mentioned on top-left. Scale bar is 5 µm.

Figure 4 shows the sintering progression at 1500°C of the relatively smaller alumina powder with 0.7 µm average size ('Al 0.7µm'). Global evaluations suggest that the sintering advances much

faster in this case, with grains increasing in size, decreasing in number and the interconnected pores turning isolated towards the end, as in Figure 4 (d). The relative densities were measured to be 89%, 92% and 94% after just 30 min, 1 hour and 10 hours respectively, indicating the final stages of sintering.

3.2 Quantitative insights

Classical parameters with regard to the evolution of the grains and the pores corresponding to all the three stages, which are extensively used in the sintering literature, were measured from the 3D data, together with the introduction of some novel parameters.

Density - Grain volume fraction correlation

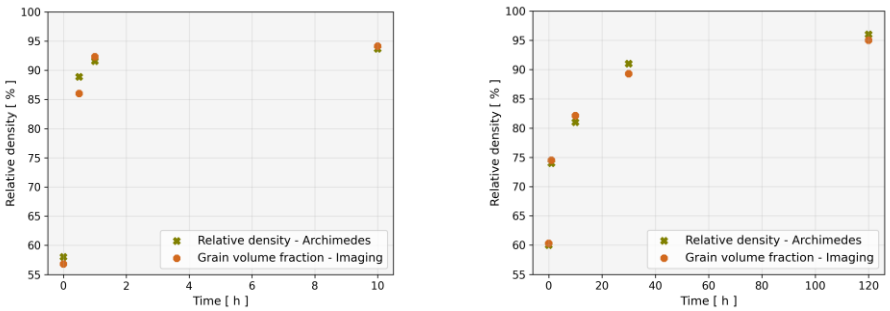

Figure 5. Correlation between the density of the sintered compact measured by the Archimedes approach and the grain volume fraction obtained by image analysis of the tomographic data for (a) Al 0.7µm and (b) Al 1.3µm, respectively.

At each time period, volume fractions of grains extracted from the 3D images, when plotted against the experimentally measured relative density values (Figure 5), show an excellent fit for most of the points for both the alumina samples. This in turn proves the effectiveness of the resolution attained, the representativeness of the ROIs and the subsequent image processing. The fit especially suggests that the samples possess a uniform green density. The agreement between the values at different time periods also provokes interchangeable usage of the terms ‘grain volume fraction’ and ‘relative density’ further in this work.

Grain size progression

Advancements in tomography techniques have led to expressing the grain growth phenomenon occurring during sintering in terms of 3D grain size distribution, replacing the earlier quantitative assessments through 2D micrographs and other stereological methods [36] [37]. Here, the grain

size deduction is carried out by granulometry measurements, as described in the previous section 2.3. Figure 6 (a) and (b) show a fairly narrow original grain size distribution, with a geometrical deviation of 1.17 and 1.2 for Al 0.7µm and Al 1.3µm respectively. De-agglomerated micron and submicron sized powders with uniform narrow size distributions are proven to improve the sinterability [38] [39] and thereby the densification of the ceramic products to more than 90%, which is very well the case in Figure 6 (a) (b) as well. Further, the curves for both the samples follow the established fact that the growth of the grains is limited in the early stages of sintering and speeds up as sintering progresses, especially after attaining over, say, 80% of the relative density.

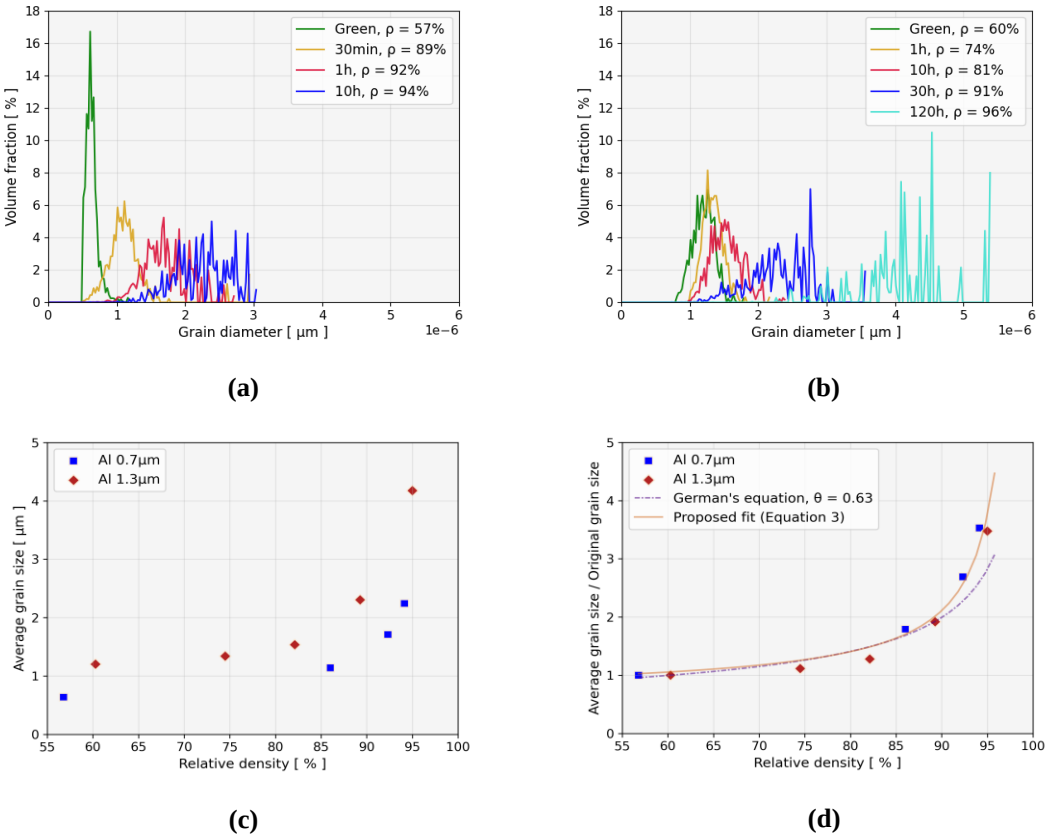

Figure 6. Evolution of grain size distribution for the two alumina samples, (a) Al 0.7µm and (b) Al 1.3µm, respectively; (c) comparison of average grain size versus density; and (d) average grain size over original grain size versus density for both these samples, along with the corresponding curve fit according to German's equation [42] **and the proposed fit.**

Also, to be noted is that these distributions do not show a distinct bimodal shape, thus indicating a pattern of normal grain growth for both the samples [3]. Average grain sizes were calculated from each of these distributions and their conformity with the scaling law proposed by Herring [40] was examined. In accordance with the analysis by Rahaman [3], this law correlates the sintering time period required to reach a given particle size, for two powders with similar shapes but different sizes (with say, radii a_1 and a_2, where $a_2 = \lambda a_1$), sintered under the same experimental conditions. The required sintering times t_2 and t_1, in this case, the time t_2 required by Al 1.3μm to produce a geometrically similar change as exhibited by Al 0.7μm in time t_1, are then interrelated as $t_2 = \lambda^{\alpha} t_1$. Here, with λ = ~2, α takes a value of around 3.5, which falls in the acceptable range of values found in the sintering literature. As per Rahaman [3], the exponent is 4 for surface diffusion and grain boundary mechanisms and 3 for lattice diffusion.

Another way of evaluating the grain growth involves plotting the evolution of the average grain size as a function of the relative density attained [41]. In fact, average grain size is considered to be the only basic microstructural descriptor necessary to evaluate the microstructural evolution in many analytical estimations. From the distributions in Figure 6 (a) (b), the average grain size points are thus extracted and plotted in Figure 6 (c). Also, the average grain size points for the two samples are divided by their original grain size and plotted against the density values as in Figure 6 (d). These points are then compared with the equation proposed by German in [42] [43] for grain size, $G = \frac{G_o \theta}{\sqrt{1-f}}$, where G_o is the initial grain size, θ is a constant with a value of 0.6, and f is the grain volume fraction. Trying different values of θ, particularly a value of 0.63 for both our samples, shows a satisfactory match, with goodness-of-fit, R^2 = ~0.8. This value of θ falls in the range of 0.41 and 0.72, as compiled in the recently conducted studies by Paredes *et al.* [44] for various samples of alumina, with different sizes, sintered at different temperatures. However, an empirical fit below (Equation 3), in line with German's equation, appears to show a better agreement. The proposed expression has an R^2 = ~0.96, with two constants, a = ~0.5 and b = ~0.4 respectively.

$$\frac{\boldsymbol{G}}{\boldsymbol{G_0}} = \mathbf{a}\,\mathbf{exp}\left(\frac{\mathbf{b}}{\sqrt{\mathbf{1}-\boldsymbol{f}}}\right) \qquad \mathbf{3}$$

Pore size measurements

During sintering, in addition to densification and the corresponding grain size evolution, changes in the pore space occur concurrently. This is evidenced by the decrease in total porosity over the sintering stages. In fact, the pore features play a key role in the physical and mechanical properties of the final sintered product. Quantification of sintering would then be best realized not only by density determinations but also by a thorough understanding of the morphological evolution of porosity in terms of pore size distribution and other associated parameters [45]. These are realized by way of granulometric analysis here, while, over the years, methods like nitrogen adsorption and mercury intrusion with commercial porosimeters were made use of [36] [46].

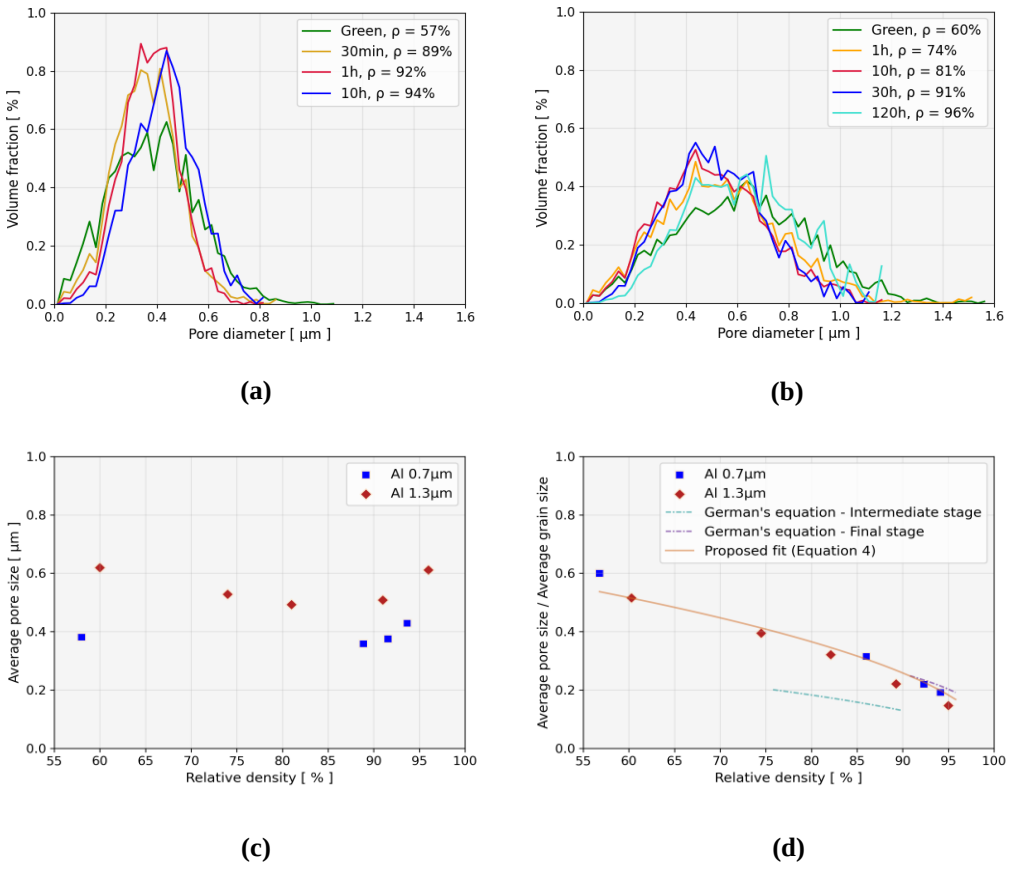

Figure 7. Evolution of pore size distribution for the two alumina samples, (a) Al 0.7µm and (b) Al 1.3µm, respectively; (c) comparison of average pore size versus density; and (d) average pore size over average grain size versus density for both these samples, along with the corresponding curve fit according to German's equations and the proposed fit.

Unlike in the grain size distributions in Figure 6 (a) (b), the pore size distribution curves rather appear to be restricted between more or less the same range of values (Figure 7 (a) (b)). Interestingly, a slight shift to the right is observed in the final curves for both the samples. The average pore size values from each of the distributions were then calculated and plotted against the relative density (Figure 7 (c)). A slight decrease in the values initially followed by an increase was observed in the case of Al 1.3µm, whereas for Al 0.7µm, there was limited variation except for the increase in the values towards the end, above 90% density, consistent with the shift observed in Figure 7 (a) (b). This increase in the average pore size at the end of sintering, as opposed to a drop as in classical theory, could be attributed to coincident grain growth, which leads to pore coalescence. The initiation of this phenomenon seems to be reflected in the sets of images in Figure 4, especially in Figure 4 (d). Further, this variation could be understood by a normalization as in Figure 7 (d), which gathers all the points for both the samples on one master curve.

Taking analytical models into consideration, porosity advancement in the intermediate stage and the final stage of sintering proposed by German [42] follows, $p = G\left(\frac{\varepsilon}{6}\right)^{1/2}$ and $p = G\left(\frac{\varepsilon}{6}\right)^{1/3}$ respectively, with a link between pore size *p,* pore volume fraction ε and grain size *G*. These analytical relations, particularly the one for intermediate stage, do not yield a good fit when compared to the values obtained in Figure 7 (c). For instance, initial pore size in Figure 7 (c) for Al 1.3µm reads 0.61 µm, whereas the porosity relation rather gives 0.3 µm instead. In order to assess this misfit, a packing of spheres with a similar grain size distribution was considered in a discrete element method (DEM) framework, as in Paredes *et al.* [44]. The packing was rendered in 3D and fed into the granulometry algorithm in GeoDict. This exercise yielded an initial average pore size value of ~0.5 µm, closer to the initial experimental value of 0.61 µm. A probable reason for the misfit could be the assumption related to geometry made in classical theories of the intermediate sintering stage. German [42] assumed grains to have the shape of a regular tetrakaidekahedron with open pore channels residing along the grain edges, as have Coble *et al.* [47] [48], Beere [49], Johnson [50] and Yan *et al.* [39]. Eudier [51] and Svoboda *et al.* [52] criticized and disapproved these models in their respective works as these assumptions were not substantiated by enough experimental justifications. Also, in addition to simple theoretical models

having a limitation in characterizing the complicated porosity behavior, unlike porosity, the definition of pore size is not so straightforward, much less its way of measurement [53].

However, a modification to the analytical expression above was found to give a rather good fit.

$$p = G\left(\frac{\varepsilon}{1.5}\right)^{1/2} \quad (4)$$

Interestingly enough, it holds true for all the stages of sintering for both the samples (Figure 7 (d)).

Pore connectivity and closure

As sintering proceeds, towards the end of the intermediate stage, open porosity gets progressively converted into closed porosity [3]. According to the observations by Coleman *et al.* [54], there exists a critical minimum grain volume fraction when the networks of interlinked, open porosity collapse to form closed, isolated pores. To track this transition, open and closed porosity values were plotted against the relative density in Figure 8 (a) for both the alumina samples.

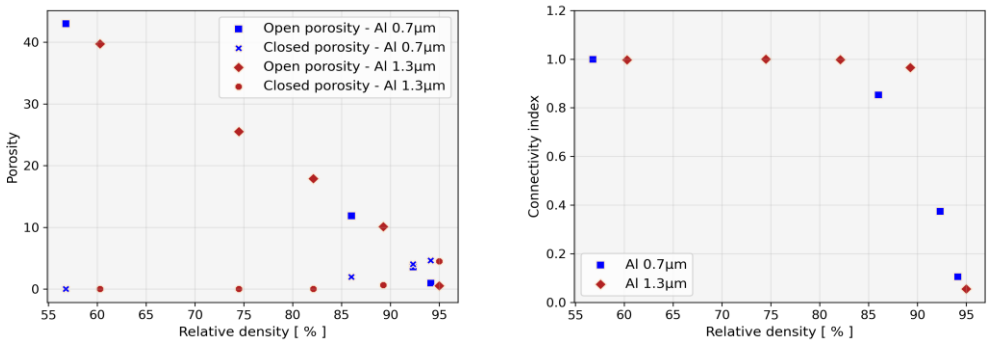

(a) **(b)**

Figure 8. Evolution of (a) open and closed porosities and (b) connectivity index values versus density for the two alumina samples, Al 0.7µm and Al 1.3µm, respectively.

The open porosity values decrease throughout for both, meaning the pore channels transform continuously into newer pore networks of lower connectivity. The closed porosity values, on the other hand, remain largely unchanged at 0 until about 85% density for Al 0.7µm and about 90% for Al 1.3µm, after which the values rise up. The plot thus gives an idea of the transition, while making it clear that the pores get fully closed at ~94-95% density for both the samples, which is the value most often reported in the literature. The fact that there is no aberration in the trajectory

of the values is also another indication of the homogeneity in the microstructure and the absence of large agglomeration [43].

Another indicator for pore closure, called connectivity index (CI) is proposed here. It is essentially the ratio of the largest pore volume over the total pore volume. The concept of CI, presented in Babin *et al.* [55], was further shown by Burr *et al.* [56] to be better suited for X-ray tomography analysis than the conventional closed porosity ratio to predict the close-off density. The advantages and drawbacks of both these methods are properly discussed in [32] and [55]. Accurate determination of pore closure requires high-resolution images, which is incompatible with large fields of view. Consequently, pores that are large with respect to the sample size could appear artificially as open porosity (intersecting the boundary of volume of interest). Closed porosity ratio is thus a biased measure with a smooth variation at pore closure. The connectivity index, meanwhile, is far less sensitive to the sample size and presents an abrupt variation at the closure. The latter is chosen here to and as shown in Figure 8 (b), the connectivity index is equal to 1 when the porosity is totally open, while it is 0 when all the pores are closed. In particular, a clear drop in the index is observed at a density between 80% and 85% for Al 0.7µm and slightly below 90% for Al 1.3µm, indicating a switch from open porosity to closed porosity. Additionally, consistent with Figure 8 (a), the pores appear to be totally closed at ~95% density.

Pore throat characterization

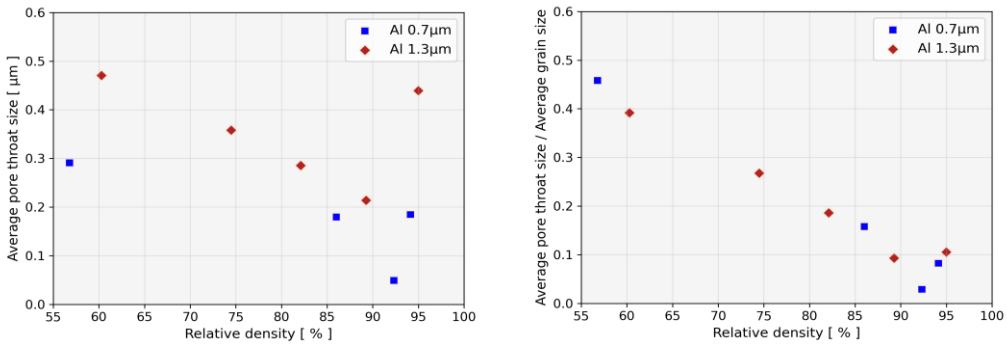

(a) **(b)**

Figure 9. (a) Comparison of average pore throat size and (b) average pore throat size over average grain size versus density for the two alumina samples, Al 0.7µm and Al 1.3µm, respectively.

As an additional analysis on the connectivity of the pores, a porosimetric investigation, outlined in section 2.3, was performed to determine pore throats. The two samples exhibit similar patterns, when the average pore throat size is plotted against density (Figure 9 (a)).

The values show a decrease throughout except a sudden increase in the end. This indicates that, at around that density, when the pores tend to close-off, most of the smaller pore throats get closed in the process, while the larger ones remain and would get closed eventually afterwards. Taking the changing grain size into consideration, as in Figure 7 (d), the points show the scaling effect and follow a master curve for both the samples in Figure 9 (b). However, above a relative density of 92%, the normalized pore throat size shows an increase while the normalized pore size does not.

3.3 Curvature maps

As illustrated in Figure 10 (a), particles in the initial stage of sintering have tiny necks in between them, with the pores mainly exhibiting a curvature opposite to the curvature of the particles. The process of sintering leads to an intensification in the neck growth phenomenon. This eventually tends to create isolated spherical pores in the final stage with an opposite curvature as against their initial curvature, as in Figure 10 (b). We expect to visualize and capture this 'concave-to-convex' transformation in the pore curvature in the course of sintering [57]. In this regard, the shape indicators, 'Shape index' and 'Curvedness', defined in Equations 1 and 2, are adopted. These shape indictors have been extensively used in the medical community [58]. Some adaptations were found in metallurgical applications as well [59]. More recently, Burr *et al.* [32] used these indicators to explore snow metamorphism.

The shape index map in Figure 10 (c), adapted from Shahani *et al.* [33] and Burr *et al.* [32], shows local shapes represented in a color scale and categorized into nine different shapes. The shape indices thus distinguish the shapes in the neighboring surface of a point. Cup-like concave shapes would have a shape index of -1, saddle-like cylindrical shapes equal to 0 and cap-like convex shapes +1.

Following the generation of pore surfaces in Avizo software and the calculation of shape indicators, these were then represented as curvature maps in the form of 2D histograms. For the 3D renderings of the image stacks of Al 1.3µm in Figure 3, the curvature maps show an evolution, as in Figure 11. These histograms are scaled with a normalized probability density P(S,C) ranging

from 0 in blue to 1 in red. In other words, regions in the map with P(S,C) =1 represent the local surfaces with the highest occurrences of the corresponding shape index and curvedness values.

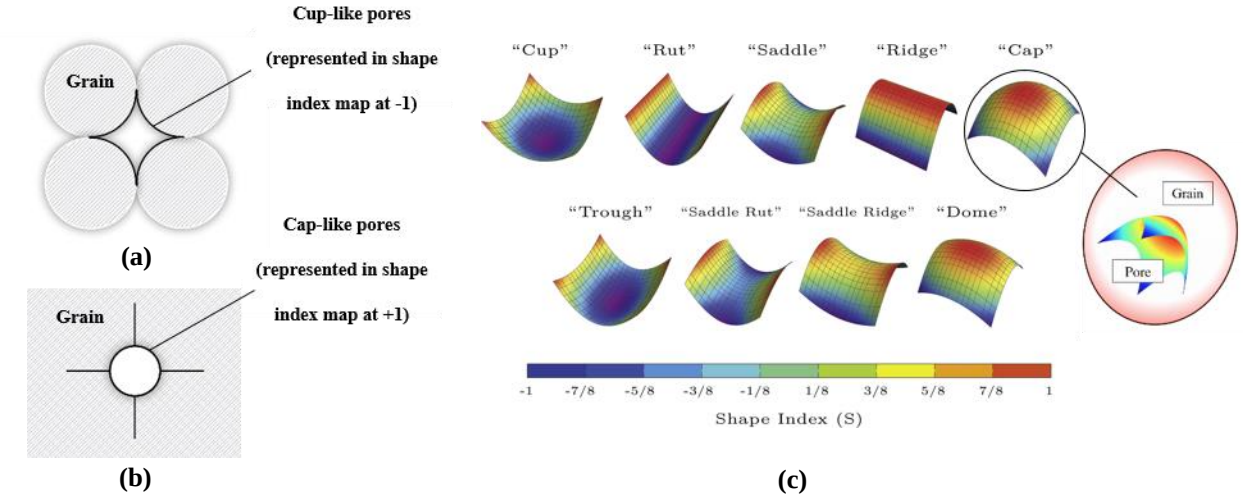

Figure 10. Representation of pore evolution during the sintering process from (a) the initial cup-like pores to (b) the final cap-like pores. (c) Shape index map showing local shapes, adapted from Shahani *et al.* [33] **and Burr *et al.*** [32]**.**

With reference to the shape index map in Figure 10 (c), the original pore network of Al 1.3µm exhibits a variety of shapes in Figure 11 (a), spanning from trough to saddle-like shapes. Eventually, with increase in time, after 30 hours of sintering in Figure 11 (d), the maximum density point P shifts to the right towards dome-like shapes, indicating that the pores are now on the verge of pinching off from the connected pore channels to become isolated.

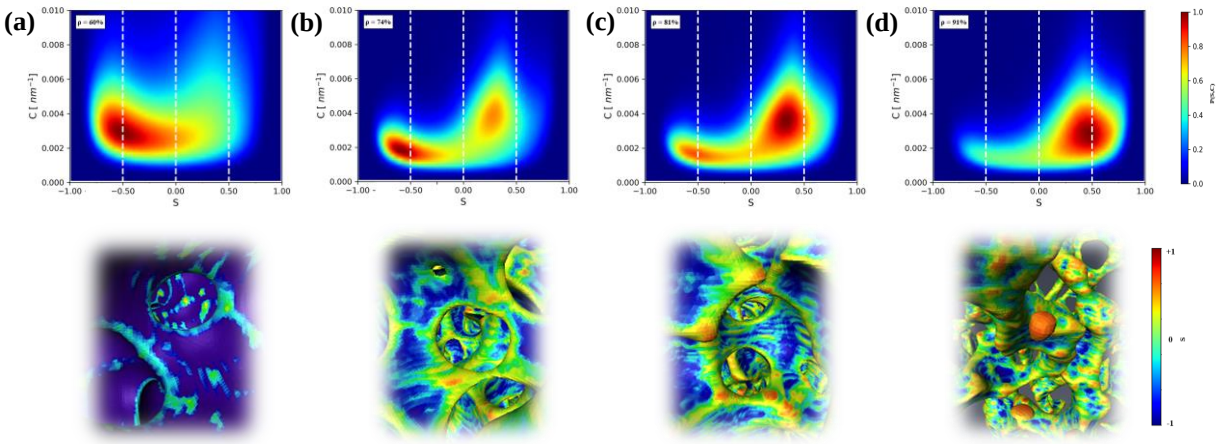

Figure 11. Pore curvature maps for 3D reconstructed alumina Al 1.3µm (in Figure 3) at (a) the initial stage and after sintering at 1500°C and observing post-mortem at (b) 1 hour, (c) 10 hours and (d) 30 hours respectively, along with snapshots of cropped sections of the 3D rendering of the pore network.

Interestingly, somewhere between relative densities of 74% and 81%, there is a clear shift in the maximum density points (Figure 11 (b) (c)).

Adjacent to each of these maps, snapshots of 3D rendering of the pore network corresponding to that particular stage are shown for better visual comprehension. These renderings display only the pore phase, with the ceramic particles appearing as void. The circular contours in the snapshots could be related to the necks between particles. Evolution of the pore curvature is clearly observed with the beginning of the development of isolated closed pores towards the end, as reflected on the shape index map.

With respect to the 3D renderings of the image stacks of Al 0.7µm in Figure 4, since the relative density reaches 89% after just 30 min and further increases progressively to 94% at the end, the curvature maps in Figure 12 have already undergone the transition observed in Figure 11 (b) (c) for Al 1.3µm. The shapes move further to the right at every stage, towards +1 of the shape index, signifying the spheroidization of pores, leading to their closure.

The values of curvedness, though, do not evolve much throughout the sintering sequence for both the samples. One could have expected a substantial increase in its values when the sintering was nearing its end, as a result of closed pore shrinkage. However, as proved by Figure 7, the pores do not show significant growth at longer times. Curvedness measurement is thus consistent with this previous result. The isolated pore in the final stage of sintering in Figure 10 (b) are hence assumed to have similar dimensional characteristics as the initial pore in Figure 10 (a), otherwise often illustrated to be much smaller in sintering literature, in the absence of grain growth.

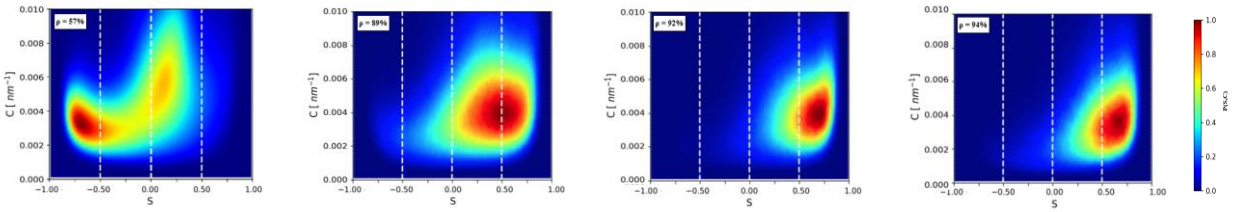

(a) **(b)** **(c)** **(d)**

Figure 12. Pore curvature maps for 3D reconstructed Al 0.7µm (in Figure 4) at (a) the initial stage and after sintering at 1500°C and observing post-mortem at (b) 30 min, (c) 1 hour and (d) 10 hours respectively.

This study therefore permits to make a proposition of classifying the stages of sintering in terms of the evolution in pore curvature. While the classical classification of a sintering process involves three sequential stages depending on parameters such as the relative density attained and other associated microstructural evolution, pore curvature advancement clearly reveals two distinct stages. The first stage is characterized by mostly cup-like pores with values of shape indices below 0 and relative densities below, say, around 80%. The second stage pertains to the latter half of the shape index map with the pore curvatures moving towards cap-like pores, after crossing 80% of the density. A transition step occurs in between these two stages, though not precisely observed in the curvature maps.

Moreover, sintering works mainly use conventional curvature parameters such as mean or Gaussian curvature (see for example Wakai *et al.* [60]). Various authors in different fields have emphasized the interest in the parameters we chose, notably Shahani *et al.* [33], for describing coarsening in solid-liquid systems. In the field of sintering, our parameters are particularly useful in the occurrence of grain growth, as the shape index is insensitive to the grain size. It thus allows for a more relevant comparison of the state of the material at various sintering times.

4. Conclusion

3D investigation of micron-sized ceramic powder systems at the particle length-scale are now feasible, thanks to the ultra-high-resolution capabilities (~25 nm voxel size) offered by upgraded synchrotron facilities. Two sets of alumina powders with particle sizes of 0.7μm and 1.3μm were sintered and observed post-mortem using the nano-CT technique at the ID16B beamline of the European synchrotron, ESRF.

Complete 3D images were obtained for these sets of powders after sintering at a given temperature for various time periods. A comprehensive quantitative analysis was performed on the evolution of grains and pores with increasing sinter density. Several classical trends and some unusual, interesting aspects occurring during the grain and pore growth kinetics were taken note of. Progression of grain growth was captured and validated with existing sintering theories. Accompanying pore growth was analyzed in terms of the changes in pore size and pore throat size. An equation to describe the pore size evolution valid for all the stages of sintering has been proposed. A connectivity index indicator was employed to trace and predict the density range at which the pore channels tend to close off.

Additionally, the data acquired from the 3D images was used to plot and analyze the so-called curvature maps. By virtue of this, a novel way of classifying the stages of sintering in relation to the advancement in pore curvature has been presented. The maps give information on the development of pore shapes throughout sintering, proving to be an indicator to track and assess the effect of sintering mechanisms on microstructural changes.

All of the information acquired may serve as datasets for the calibration of numerical models and for testing their veracity.

However, subtler but important effects at the local level go unnoticed in global analyses. Therefore, further thorough research including many more sintering parameters is needed in order to take into account the collective behavior occurring in a sintering process and to validate the obtained results. A real-time in-situ tracking of the sintering progression at a similar resolution scale could bring about a substantial improvement in this regard, by exploring relevant details and associated parameters at the particle length-scale. An in-situ analysis would also enable tracking of initial (and perhaps intermediate) stages of sintering by segmenting individual features. These aspects are being dealt with in our ongoing research.

Acknowledgements

This project has received funding from the European Union's Horizon 2020 research and innovation programme under the Marie Skłodowska-Curie grant agreement MATHEGRAM No 813202. The authors also thank the ESRF for the provision of synchrotron radiation facilities (Proposal MA4632).

References

[1] R. K. Bordia, S. J. L. Kang, and E. A. Olevsky, "Current understanding and future research directions at the onset of the next century of sintering science and technology," *Journal of the American Ceramic Society*, vol. 100, no. 6, pp. 2314–2352, Jun. 2017, doi: 10.1111/jace.14919.

[2] S.-J. L. Kang, *Sintering: densification, grain growth and microstructure*. Elsevier, 2005.

[3] M. N. Rahaman, *Ceramic processing and sintering*. CRC press, 2003.

[4] B. Otsuki, M. Takemoto, S. Fujibayashi, M. Neo, T. Kokubo, and T. Nakamura, "Pore throat size and connectivity determine bone and tissue ingrowth into porous implants:

Three-dimensional micro-CT based structural analyses of porous bioactive titanium implants," *Biomaterials*, vol. 27, no. 35, pp. 5892–5900, Dec. 2006, doi: 10.1016/j.biomaterials.2006.08.013.

[5] W. Zhang, K. E. Thompson, A. H. Reed, and L. Beenken, "Relationship between packing structure and porosity in fixed beds of equilateral cylindrical particles," 2006, doi: 10.1016/j.

[6] W. Pabst, E. Gregorová, I. Sedlářová, and M. Černý, "Preparation and characterization of porous alumina-zirconia composite ceramics," *J Eur Ceram Soc*, vol. 31, no. 14, pp. 2721–2731, Nov. 2011, doi: 10.1016/j.jeurceramsoc.2011.01.011.

[7] O. Lame, D. Bellet, M. Di Michiel, and D. Bouvard, "Bulk observation of metal powder sintering by X-ray synchrotron microtomography," *Acta Mater*, vol. 52, no. 4, pp. 977–984, Feb. 2004, doi: 10.1016/j.actamat.2003.10.032.

[8] M. Nöthe, M. Schulze, R. Grupp, B. Kieback, and A. Haibel, "Investigation of Sintering of Spherical Copper Powder by Micro Focus Computed Tomography (μCT) and Synchrotron Tomography," *Materials Science Forum*, vol. 539–543, pp. 2657–2662, Mar. 2007, doi: 10.4028/www.scientific.net/msf.539-543.2657.

[9] L. Olmos *et al.*, "Analysing the sintering of heterogeneous powder structures by in situ microtomography," *Philosophical Magazine*, vol. 89, no. 32, pp. 2949–2965, Nov. 2009, doi: 10.1080/14786430903150225.

[10] B. Kieback, M. Nöthe, J. Banhart, and R. Grupp, "Investigation of sintering processes by tomography," in *Materials Science Forum*, Trans Tech Publications Ltd, 2010, pp. 2511–2516. doi: 10.4028/www.scientific.net/MSF.638-642.2511.

[11] F. Delannay and J. M. Missiaen, "Experimental validation of a new model for the initial stage of sintering of single phase systems," *Acta Mater*, vol. 57, no. 2, pp. 420–431, 2009, doi: 10.1016/j.actamat.2008.09.019.

[12] D. Bernard, D. Gendron, J. M. Heintz, S. Bordère, and J. Etourneau, "First direct 3D visualisation of microstructural evolutions during sintering through X-ray computed microtomography," *Acta Mater*, vol. 53, no. 1, pp. 121–128, Jan. 2005, doi: 10.1016/j.actamat.2004.09.027.

[13] P. Lu, J. J. Lannutti, P. Klobes, and K. Meyer, “X-ray computed tomography and mercury porosimetry for evaluation of density evolution and porosity distribution,” *Journal of the American Ceramic Society*, vol. 83, no. 3, pp. 518–522, 2000, doi: 10.1111/j.1151-2916.2000.tb01227.x.

[14] F. Xu, X. F. Hu, H. Miao, and J. H. Zhao, “In situ investigation of ceramic sintering by synchrotron radiation X-ray computed tomography,” *Opt Lasers Eng*, vol. 48, no. 11, pp. 1082–1088, Nov. 2010, doi: 10.1016/j.optlaseng.2009.12.012.

[15] G. Okuma *et al.*, “Microstructural evolution of electrodes in sintering of multi-layer ceramic capacitors (MLCC) observed by synchrotron X-ray nano-CT,” *Acta Mater*, vol. 206, Mar. 2021, doi: 10.1016/j.actamat.2020.116605.

[16] J. Villanova *et al.*, “Fast in situ 3D nanoimaging: a new tool for dynamic characterization in materials science,” *Materials Today*, vol. 20, no. 7, pp. 354–359, Sep. 2017, doi: 10.1016/j.mattod.2017.06.001.

[17] L. Salvo, M. Suéry, A. Marmottant, N. Limodin, and D. Bernard, “3D imaging in material science: Application of X-ray tomography,” *Comptes Rendus Physique*, vol. 11, no. 9–10. Elsevier Masson SAS, pp. 641–649, 2010. doi: 10.1016/j.crhy.2010.12.003.

[18] P. Cloetens *et al.*, “Holotomography: Quantitative phase tomography with micrometer resolution using hard synchrotron radiation x rays,” *Appl Phys Lett*, vol. 75, no. 19, pp. 2912–2914, Nov. 1999, doi: 10.1063/1.125225.

[19] G. Martinez-Criado *et al.*, “ID16B: A hard X-ray nanoprobe beamline at the ESRF for nano-analysis,” in *Journal of Synchrotron Radiation*, International Union of Crystallography, 2016, pp. 344–352. doi: 10.1107/S1600577515019839.

[20] S. Fujiwara, Y. Tamura, H. Maki, N. Azuma, and Y. Takeuchi, “Development of New High-Purity Alumina, ‘SUMITOMO KAGAKU’, vol. 2007-I.,” 2007.

[21] S. Sakamoto, T. Kajino, T. Nasu, S. Sakaki, and Y. Sakatani, “New Technology and Application Development of High Purity Alumina, ‘SUMITOMO KAGAKU’, vol. 2020.,” 2020.

[22] Y. Cheng *et al.*, “Direct three-dimensional imaging of polymer-water interfaces by nanoscale hard X-ray phase tomography,” *Soft Matter*, vol. 10, no. 17, pp. 2982–2990, May 2014, doi: 10.1039/c3sm52604f.

[23] B. Yu *et al.*, “Phase retrieval in 3D X-ray magnified phase nano CT: Imaging bone tissue at the nanoscale,” in *Proceedings - International Symposium on Biomedical Imaging*, IEEE Computer Society, Jun. 2017, pp. 56–59. doi: 10.1109/ISBI.2017.7950467.

[24] A. Mirone, E. Brun, E. Gouillart, P. Tafforeau, and J. Kieffer, “The PyHST2 hybrid distributed code for high speed tomographic reconstruction with iterative reconstruction and a priori knowledge capabilities,” *Nucl Instrum Methods Phys Res B*, vol. 324, pp. 41–48, Apr. 2014, doi: 10.1016/j.nimb.2013.09.030.

[25] A. Lyckegaard, G. Johnson, and P. Tafforeau, “Correction of ring artifacts in X-ray tomographic images Palaeopathology of South African early hominins View project The 1st France-Myanmar Irrawaddy fossil expedition in 2007 View project Correction of Ring Artifacts in X-ray Tomographic Images,” 2011. [Online]. Available: https://www.researchgate.net/publication/283832650

[26] J. Schindelin *et al.*, “Fiji: An open-source platform for biological-image analysis,” *Nature Methods*, vol. 9, no. 7. pp. 676–682, Jul. 2012. doi: 10.1038/nmeth.2019.

[27] J. Becker *et al.*, “GeoDict (Release 2022) [Simulation software], Math2Market GmbH”.

[28] “GrainFind handbook, in GeoDict 2022 User Guide from Math2Market GmbH, Germany.” doi: doi.org/10.30423/userguide.geodict2022.

[29] “PoroDict handbook, in GeoDict 2022 User Guide from Math2Market GmbH, Germany ”.

[30] V. Boulos, V. Fristot, D. Houzet, L. Salvo, and P. Lhuissier, “Investigating performance variations of an optimized GPU-ported granulometry algorithm,” 2012.

[31] J. J. Koenderink and A. J. Van Doorn, “Surface shape and curvature scales.”

[32] A. Burr, P. Lhuissier, C. L. Martin, and A. Philip, “In situ X-ray tomography densification of firn: The role of mechanics and diffusion processes,” *Acta Mater*, vol. 167, pp. 210–220, Apr. 2019, doi: 10.1016/j.actamat.2019.01.053.

[33] A. J. Shahani, E. B. Gulsoy, V. J. Roussochatzakis, J. W. Gibbs, J. L. Fife, and P. W. Voorhees, “The dynamics of coarsening in highly anisotropic systems: Si particles in Al-Si liquids,” *Acta Mater*, vol. 97, pp. 325–337, Jul. 2015, doi: 10.1016/j.actamat.2015.06.064.

[34] “Avizo 2021.1. https://www.fei.com/software/avizo-formaterials- science.”

[35] N. P. Bansal and A. R. Boccaccini, *Ceramics and composites processing methods*. John Wiley & Sons, 2012.

[36] T. -S Yeh and M. D. Sacks, “Effect of Particle Size Distribution on the Sintering of Alumina,” *Journal of the American Ceramic Society*, vol. 71, no. 12, p. C-484-C-487, 1988, doi: 10.1111/j.1151-2916.1988.tb05812.x.

[37] I. Borgh *et al.*, “Microstructure, grain size distribution and grain shape in WC-Co alloys sintered at different carbon activities,” *Int J Refract Metals Hard Mater*, vol. 43, pp. 205–211, 2014, doi: 10.1016/j.ijrmhm.2013.12.007.

[38] U. Chowdhry and R. M. Cannon, *Microstructural evolution during the processing of sodium β-alumina. In Processing of Crystalline Ceramics (pp. 443-455).* . Springer, Boston, MA., 1978.

[39] M. F. Yan, R. M. Cannon, H. K. Bowen, and U. Chowdhry, “Effect of Grain Size Distribution on Sintered Density.”

[40] C. Herring, “Effect of change of scale on sintering phenomena,” *J Appl Phys*, vol. 21, no. 4, pp. 301–303, 1950, doi: 10.1063/1.1699658.

[41] I. Nettleship, R. J. McAfee, and W. S. Slaughter, “Evolution of the grain size distribution during the sintering of alumina at 1350°C,” *Journal of the American Ceramic Society*, vol. 85, no. 8, pp. 1954–1960, 2002, doi: 10.1111/j.1151-2916.2002.tb00387.x.

[42] R. M. German, “Coarsening in sintering: Grain shape distribution, grain size distribution, and grain growth kinetics in solid-pore systems,” *Critical Reviews in Solid State and Materials Sciences*, vol. 35, no. 4, pp. 263–305, Oct. 2010, doi: 10.1080/10408436.2010.525197.

[43] R. German, *Sintering: from empirical observations to scientific principles* . Butterworth-Heinemann, 2014.

[44] B. Paredes-Goyes, D. Jauffres, J. M. Missiaen, and C. L. Martin, “Grain growth in sintering: A discrete element model on large packings,” *Acta Mater*, vol. 218, Oct. 2021, doi: 10.1016/j.actamat.2021.117182.

[45] J. A. Varela, O. J. Whittemore, and E. Longo, “Pore Size Evolution during Sintering of Ceramic Oxides,” 1990.

[46] - J Whi’itemore and J.-J. Sipe, “Pore Growth during the Initial Stages of Sintering Ceramics*,” Elsevier Sequoia S.A, 1974.

[47] R. L. COBLE and W. D. KINGERY, “Effect of Porosity on Physical Properties of Sintered Alumina,” *Journal of the American Ceramic Society*, vol. 39, no. 11, pp. 377–385, 1956, doi: 10.1111/j.1151-2916.1956.tb15608.x.

[48] R. L. Coble and T. K. Gupta, *pp. 423–41 in Sintering and Related Phenomena*. Gordon and Breach, Science Publishers, Inc., New York., 1967.

[49] W. Beere, “The second stage sintering kinetics of powder compacts,” *Acta Metallurgica*, vol. 23, no. 1, pp. 139–145, 1975, doi: 10.1016/0001-6160(75)90079-6.

[50] D. L. JOHNSON, “A General Model for the Intermediate Stage of Sintering,” *Journal of the American Ceramic Society*, vol. 53, no. 10, pp. 574–577, 1970, doi: 10.1111/j.1151-2916.1970.tb15969.x.

[51] M. Eudier, *pp. 442 in Sintering and Related Phenomena.* . Gordon and Breach, “Science Publishers Inc., New York, 1967.

[52] J. Svobodat, H. Riedel, and H. Zipse, “Equilibrium pore surfaces, sintering stresses and constitutive equations for the intermediate and late stages of sintering—I. computation of equilibrium surfaces,” *Acta metall, mater*, vol. 42, no. 2, pp. 435–443, 1994.

[53] J. R. Nimmo, “Porosity and Pore Size Distribution,” in *Reference Module in Earth Systems and Environmental Sciences*, Elsevier, 2013. doi: 10.1016/b978-0-12-409548-9.05265-9.

[54] S. C. Coleman and W. B. Beeré, “The sintering of open and closed porosity in UO2,” *Philosophical Magazine*, vol. 31, no. 6, pp. 1403–1413, 1975, doi: 10.1080/00318087508228691.

[55] P. Babin *et al.*, “Fast X-ray tomography analysis of bubble growth and foam setting during breadmaking,” *J Cereal Sci*, vol. 43, no. 3, pp. 393–397, May 2006, doi: 10.1016/j.jcs.2005.12.002.

[56] A. Burr, C. Ballot, P. Lhuissier, P. Martinerie, C. L. Martin, and A. Philip, “Pore morphology of polar firn around closure revealed by X-ray tomography,” *Cryosphere*, vol. 12, no. 7, pp. 2481–2500, Jul. 2018, doi: 10.5194/tc-12-2481-2018.

[57] A. M. Venkatesh, D. Bouvard, P. Lhuissier, and J. Villanova, “Analysis of Pore Evolution During Ceramic Powder Sintering by Synchrotron X-ray Nano-Tomography,” in *Advances in Powder Metallurgy & Particulate Materials—2022*, U.S.A: Metal Powder Industries Federation, 2022.

[58] H. H. Hu, H. Y. Chen, C. I. Hung, W. Y. Guo, and Y. Te Wu, “Shape and curvedness analysis of brain morphology using human fetal magnetic resonance images in utero,” *Brain Struct Funct*, vol. 218, no. 6, pp. 1451–1462, Nov. 2013, doi: 10.1007/s00429-012-0469-3.

[59] J. W. Gibbs *et al.*, “The Three-Dimensional Morphology of Growing Dendrites,” *Sci Rep*, vol. 5, Jul. 2015, doi: 10.1038/srep11824.

[60] G. Okuma, D. Kadowaki, T. Hondo, S. Tanaka, and F. Wakai, “Interface topology for distinguishing stages of sintering,” *Sci Rep*, vol. 7, no. 1, p. 11106, Sep. 2017, doi: 10.1038/s41598-017-11667-2.